Spin-orbit-coupling-induced band splitting in two-dimensional hybrid organic-inorganic perovskites: Importance of organic cations

Sampreeti Bhattacharya [1] and Yosuke Kanai [1,2,*]

[1]Department of Chemistry, University of North Carolina at Chapel Hill, Chapel Hill 27599, North Carolina, USA
[2]Department of Physics and Astronomy, University of North Carolina at Chapel Hill, Chapel Hill 27599, North Carolina, USA

(Received 17 January 2023; revised 11 April 2023; accepted 19 April 2023; published 2 May 2023)

We investigate how the spin-orbit-coupling-induced lifting of the spin degeneracy depends indirectly on constituting organic motifs in two-dimensional hybrid organic-inorganic perovskites. We examine experimentally synthesized structures using first-principles electronic structure theory. In particular, the effect of the organic spacer cation packing and of the methyl ammonium orientation within the inorganic layer are elucidated. Both the organic spacer packing and subtle changes in methyl ammonium orientations can cause enough distortions of lead iodide octahedral cages to induce the spin splitting. Interestingly, the momentum-independent persistent spin texture splitting rather than the traditional Rashba/Dresselhaus splitting is observed for a structure in which organic spacer molecules are modified with fluorine substitution. Our calculation on these experimentally reported structures highlights the important role of the organic constituents in these hybrid organic inorganic perovskites for the spin splitting.

DOI: 10.1103/PhysRevMaterials.7.055001

I. INTRODUCTION

Two-dimensional (2D) hybrid organic inorganic perovskites (HOIPs) have received significant interest in recent years for optoelectronic and spintronic devices [1–5]. A range of properties exhibited by the HOIPs have sparked widespread interest of their use in technological development in various energy-related fields [6–8]. Owing to the multiple-quantum-well-like structure [9], these materials can be engineered on the molecular level to achieve desirable physical properties, for example, an increased photovoltaic efficiency through enhanced carrier lifetime [10]. Such tunability of material properties for 2D HOIPs can be achieved by a plethora of chemical and structural variations. Key electronic structure properties can be controlled by introducing octahedral distortions in a lead iodide (PbI) inorganic sublattice of 2D HOIPs, transmuting magnetic and electronic degrees of freedom [11]. Lifting of the spin degeneracy for the conduction band states by spin-orbit coupling (SOC) is a particularly important example of such ideas, and the band splitting has received great attention in recent years because of its technological applications [12–15]. The crystal symmetry is inherently related to this particularly important property, and it is highly susceptible to the PbI octahedral cage structures in the inorganic layer.

Distortions and dislocations of atoms in organic or inorganic sublattices collectively affect the overall space group of 2D HOIPs, inducing symmetry breaking in the PbI octahedral cages. Interestingly, modifying organic spacer cations with substituent atoms/groups [16–18] or changing the stereochemistry of the spacer cations results in an R-/S-structural chirality transfer to the inorganic layer [19]. Increasing the numbers of layers, n, of inorganic sublattice can also induce PbI octahedral distortions, leading to systematic changes to the crystal symmetry [20]. In 2D inorganic oxide perovskites [21], local electronic polarization is observed in the lateral direction due to octahedral distortions for even-layered inorganic sublattices [11,20], and the layer dependence of octahedral distortions in 2D HOIPs with $n = 1, 2, 3$ could follow such a trend, albeit more complex in nature and origin. The octahedral distortions are often referred to as Glazer modes [22], and they are particularly important for understanding SOC effect in 2D HOIPs. These distortions lower the symmetry of the structure [21], and are directly related to the symmetry-governed SOC effect. As discussed in the work by Zhang *et al.* [23], the band splitting in periodic lattice is not exclusively dependent on the global space group but rather is dependent on the site symmetry of the individual atoms. The atoms in a noncentrosymmetric site can contribute to symmetry breaking, irrespective of the nature of the overall space group. In this paper, we elucidate the interdependence of electronic structure on crystal geometry, particularly unraveling how organic spacer cations as well as methyl ammonium (MA) orientations affect the electronic structure property, particularly the band splitting, via lowering the local symmetry of a PbI inorganic sublattice. To this end, large-scale first-principles calculations are performed on n-layered phenylethylammonium (PEA) PbI perovskites, whose experimentally determined structures are reported in the literature.

II. RASHBA/DRESSELHAUS EFFECT

In first-principles calculations, relativistic treatment of the Schrödinger's equation is an essential aspect for studying SOC-induced band splitting. Under the relativistic

*Corresponding author: ykanai@unc.edu

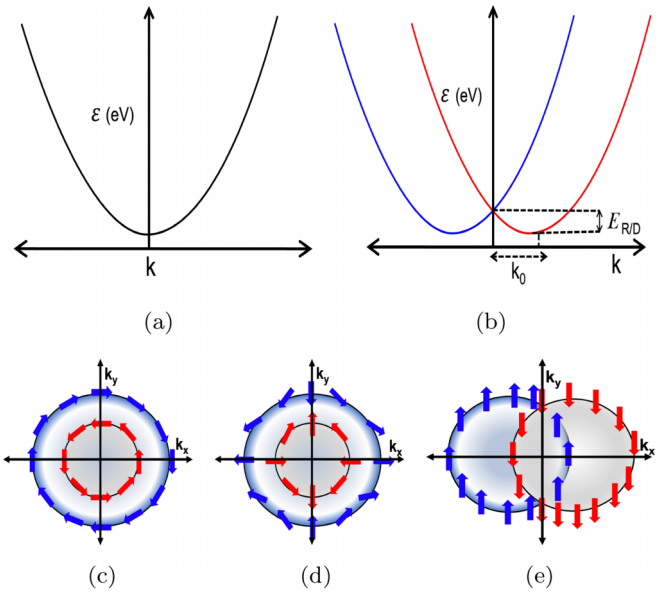

FIG. 1. (a) A schematic representation of doubly degenerate conduction band at $\mathbf{k} = 0$. (b) Spin split bands along the high-symmetry k path. $E_{\mathbf{R/D}}$ is the splitting energy and k_0 is the resulting change in the momentum for the energy minimum [35]. Schematics of the spin texture for (c) Rashba, (d) Dresselhaus, and (e) persistent spin splitting, respectively. The blue and red arrows show the resulting spin directions in the outer and inner bands, respectively.

formulation, the equation is reduced so one approximates the Dirac equation with the relativistic Kohn-Sham equation, and the density-dependent single-particle Hamiltonian is given by

$$\begin{aligned}\hat{H} &= \hat{t}_{\mathrm{SR}} + \hat{v}_{\mathrm{ext}} + \hat{v}_{es} + \hat{v}_{\mathrm{xc}} + \hat{v}_{\mathrm{SOC}} \\ &= \hat{t}_{\mathrm{SR}} + \hat{v} + \hat{v}_{\mathrm{SOC}}, \end{aligned} \tag{1}$$

where $\hat{t}_{\mathrm{SR}}$ is the scalar relativistic kinetic energy operator, $\hat{v}_{\mathrm{ext}}$ is the external potential, $\hat{v}_{\mathrm{es}}$ is the electrostatic potential, and $\hat{v}_{\mathrm{xc}}$ is the exchange correlation operator. The effective Kohn-Sham potential, $\hat{v}$, is defined to include all these individual potential energy terms. The SOC operator $\hat{v}_{\mathrm{SOC}}$ is given by

$$\hat{v}_{\mathrm{SOC}} = \frac{i}{4c^2}\hat{\boldsymbol{\sigma}} \cdot (\hat{\boldsymbol{p}}\hat{v} \times \hat{\boldsymbol{p}}), \tag{2}$$

where $\hat{\boldsymbol{p}} = -i\nabla$ is the momentum operator and $\hat{\boldsymbol{\sigma}}$ are Pauli spin matrices. The SOC plays a central role in determining electronic properties of 2D HOIPs due to the presence of Pb atoms, which gives a strong contribution to the conduction band edge. For all systems discussed in this paper, the conduction band edges derive mainly from Pb $6p$ states, and thus are largely affected by the SOC. With the SOC operator $\hat{v}_{\mathrm{SOC}}$ present, the usual independent spin-up and spin-down states are no longer the eigenstates of the Hamiltonian. Instead, resulting eigenstates (i.e., spinors) are generally expressed as $\psi_{n\mathbf{k},\chi^{+/-}}(\mathbf{r}) = \psi^{\alpha}_{n\mathbf{k}}(\mathbf{r})|\uparrow\rangle + \psi^{\beta}_{n\mathbf{k}}(\mathbf{r})|\downarrow\rangle$, and $\chi^{+/-}$ indicates the quantum number for the two spin degrees of freedom. At the same time, the time-reversal symmetry [i.e., $\epsilon_{\chi^+}(\mathbf{k}) = \epsilon_{\chi^-}(-\mathbf{k})$] still holds, and having the inversion symmetry in a crystal [i.e., $\epsilon_{\chi^+}(\mathbf{k}) = \epsilon_{\chi^+}(-\mathbf{k})$] results in

$$\epsilon_{\chi^-}(\mathbf{k}) = \epsilon_{\chi^+}(\mathbf{k}). \tag{3}$$

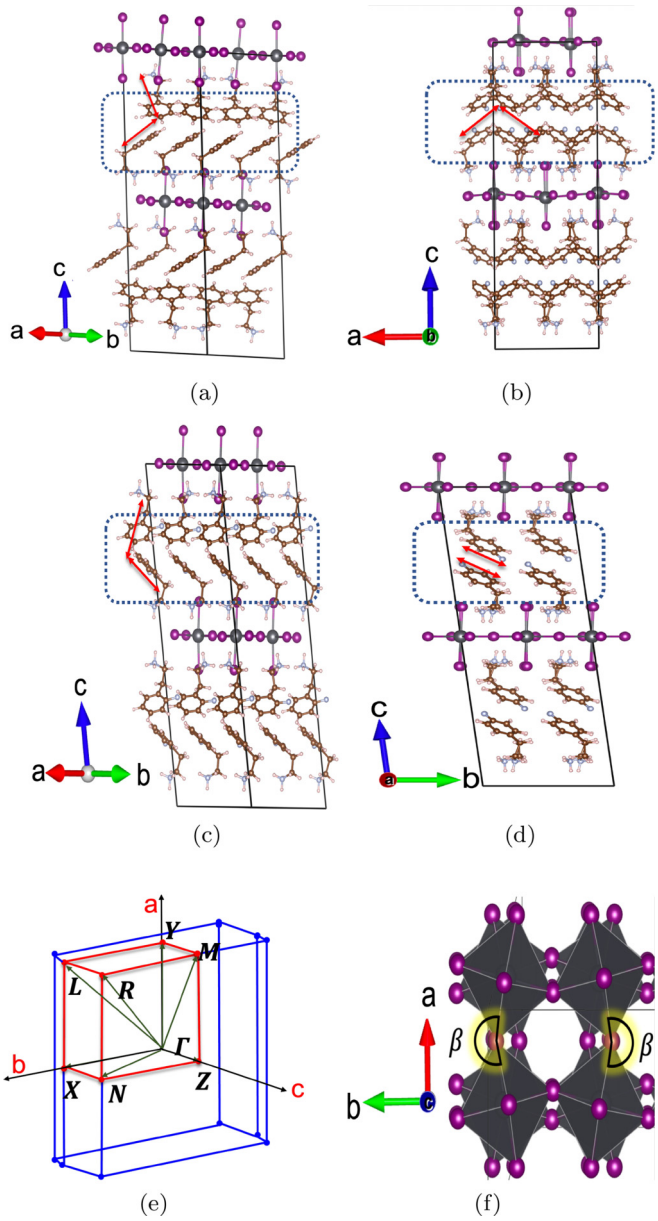

FIG. 2. Structures of (a) $(PEA)_2PbI_4$, (b) $(m\text{-}FPEA)_2PbI_4$, (c) $(o\text{-}FPEA)_2PbI_4$, and (d) $(p\text{-}FPEA)_2PbI_4$. A corresponding Brillouin zone for $(x\text{-}FPEA)_2PbI_4$ including high-symmetry k paths from $X - \Gamma - Y$ is shown in (e). The angles of orientation between the two PEAs in the organic layers (blue dotted box) are $\approx 90^\circ$ (perpendicular) for (a) $(PEA)_2PbI_4$. (f) Glazer mode distortion [aac^-] shown along the c [001] direction. The lateral Pb–I–Pb bond angles in the inorganic layers β and β' are used in Ref. [32] as a key indicator metric for band dispersion. In (b) $(m\text{-}FPEA)_2PbI_4$, the molecules are in a gauche-type arrangement, as reported in Ref. [16]. (c) $(o\text{-}FPEA)_2PbI_4$, the angles between the parallel and perpendicular arrangements. For (d) PEA, the organic molecules are oriented in parallel with the maximum π-π interaction (parallel).

Thus, even with SOC, the electronic states abide spatiosymmetric relation (spin degeneracy) such that the energy bands at the same $\mathbf{k}$ have twofold degeneracy when the inversion symmetry is present. However, in spatially noncentrosymmetric systems, the time-reversal degeneracy is not valid [24],

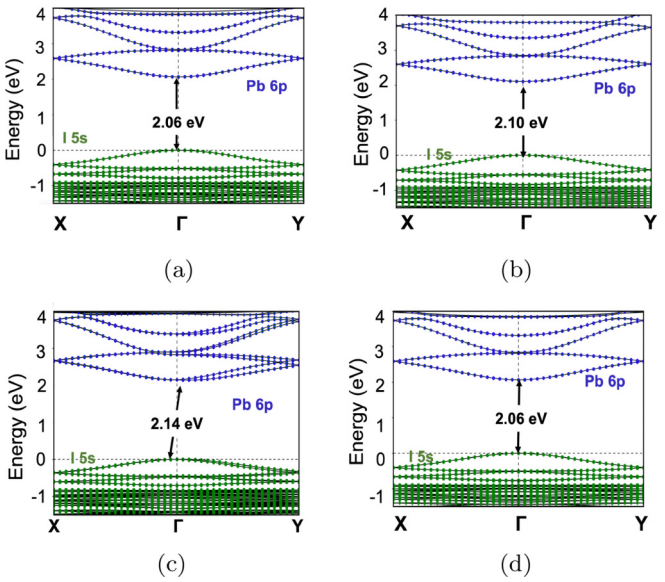

FIG. 3. Band structure for (a) $(PEA)_2PbI_4$, (b) $(m\text{-}FPEA)_2PbI_4$, (c) $(o\text{-}FPEA)_2PbI_4$, and (d) $(p\text{-}FPEA)_2PbI_4$ along the selected high-symmetry $X-\Gamma-Y$ path. Contributions from Pb $6p$ and I $5p$ states are highlighted in blue and green colors, respectively.

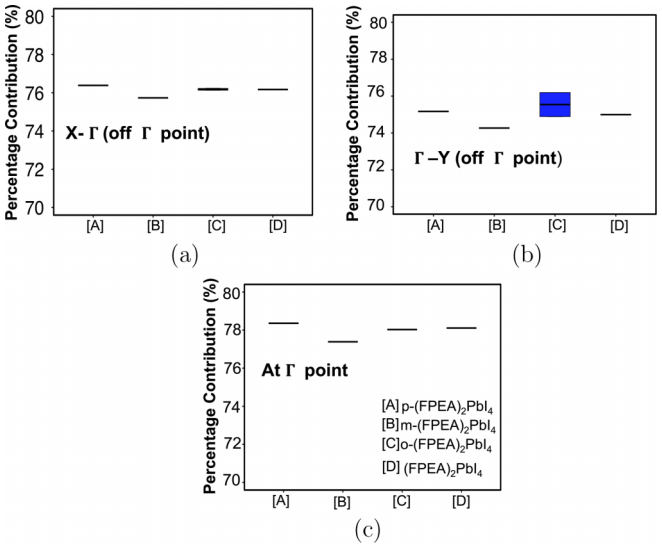

FIG. 5. Percentage contributions of Pb atomic orbitals to the conduction band minimum (CBM) states are shown for (a) off Γ point along $X-\Gamma$ k-path by 0.072 $Å^{-1}$, (b) at Γ point, and (c) off Γ point along $\Gamma-Y$ k-path by 0.072 $Å^{-1}$ for $(p\text{-}FPEA)_2PbI_4$, $(m\text{-}FPEA)_2PbI_4$, $(o\text{-}FPEA)_2PbI_4$, and $(FPEA)_2PbI_4$ shown in the horizontal axis. The same magnitudes of the Pb contributions to the four CBM states are shown as black lines. The blue rectangle for the system indicates a varying degree of contributions from different Pb atoms to the CBM states.

and the lack thereof results in a **k** (momentum)-dependent spin-splitting of the otherwise spin degenerate states as shown schematically in Figs. 1(a) and 1(b). Such momentum-dependent splittings are often referred to as Rashba or Dresselhaus splittings. For the 2D electron gas [25], the SOC yields a simple band dispersion relationship, $\epsilon^{\pm}(\mathbf{k}) = (\frac{\mathbf{k}^2}{2m^*}) \pm \alpha_{\mathbf{R/D}}|\mathbf{k}|$. The band splitting parameter, $\alpha_{\mathbf{R/D}}$, can then be written as $\alpha_{\mathbf{R/D}} = \frac{2E_{\mathbf{R/D}}}{k_0}$, where $E_{\mathbf{R/D}}$ is the band splitting parameter [26], as shown in Fig. 1(b).

In homogeneous systems, Rashba and Dresselhaus spin splittings can be a consequence of a bulk inversion asymmetry of the underlying crystal (e.g., a zinc blende structure [27]), and/or of a structure inversion asymmetry of the confinement potential, respectively [28,29]. However, for heterogeneous systems like HOIPs, such a classification is not suitable, and both local and global site asymmetries as well as a local dipole determine the existence of Rashba- or Dresselhaus-type

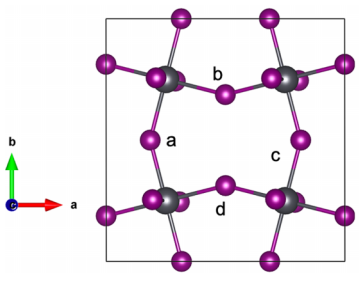

Crystal Geometry	$\theta_{i=\{a,b,c,d\}}$ (degree)	δ_{ac}	δ_{bd}
$(PEA)_2PbI_4$	a=149.09 b=149.10 c=149.09 d=149.10	0.0	0.0
$(p\text{-}FPEA)_2PbI_4$	a=149.41 b=149.42 c=149.42 d=149.41	0.0	0.0
$(m\text{-}FPEA)_2PbI_4$	a=147.16 b=147.67 c=147.21 d=147.70	0.05	0.03
$(o\text{-}FPEA)_2PbI_4$	a=142.86 b=149.36 c=152.24 d=148.72	9.38	0.64

FIG. 4. PbI cage structure viewed from c [001] direction, with the lateral angles characterized by $\theta_{i=\{a,b,c,d\}}$. Corresponding opposite angle differences are summarized for $(PEA)_2PbI_4$, $(p\text{-}FPEA)_2PbI_4$, $(m\text{-}FPEA)_2PbI_4$, and $(o\text{-}FPEA)_2PbI_4$ as a table. The opposite angle differences δ_{ac} and δ_{bd} are calculated as $|\theta_a - \theta_c|$ and $|\theta_b - \theta_d|$, respectively.

splittings [23]. For HOIPs of the 2D quantum well type [9], structural inversion symmetry is absent in the stacking axis (c direction in this paper). The classification of the spin-splitting is more suitably given in terms of the underlying model Hamiltonian for the SOC effect. The contribution from SOC can be expressed as the SOC Hamiltonian in

$$H_{\mathrm{SOC}} = \Omega(\mathbf{k}) \cdot \sigma, \tag{4}$$

where σ is the Pauli spin matrix. $\Omega(\mathbf{k})$ can take different forms, depending on the spin-splitting type [30]. For example, in the cases of Rashba and Dresselhaus types of splitting, this **k**-dependent field is a function of both k_x and k_y [i.e., $\Omega(\mathbf{k}) = \Omega(k_x, k_y, 0)$] [31]. Such momentum-dependent Rashba-/Dresselhaus-type splittings (see Fig. 1) can be often found in HOIPs [19,32]. Additionally, in the case of unidirectional SOC-induced band splitting, recently observed for a 2D HOIP [33], the associated SOC field takes the form of either $\Omega(\mathbf{k}) = \Omega(k_x, 0, 0)$ or $\Omega(0, k_y, 0)$. This understanding from the SOC model Hamiltonian can be connected to the first-principles theory by calculating the expectation value of Pauli spin operator, or simply referred to as spin texture (i.e., $\sigma_{i,n\mathbf{k}} = \langle\psi_{n\mathbf{k}}|\hat{\sigma}_i|\psi_{n\mathbf{k}}\rangle$, where $i = x, y, z$). Spin texture shows a helical shape in the $k_{x,y}$ plane, depending on the type of spin splitting and the site symmetry around the high symmetry k point [34]. The directions of the corresponding spin texture are perpendicular to the wave vector given by the result of k_x and k_y for Rashba-type splittings, as shown in Fig. 1(c). For Dresselhaus-type splitting, the spin texture at k_x and k_y axes are parallel to the axes, as shown in Fig. 1(d). For the particularly interesting case of the unidirectional

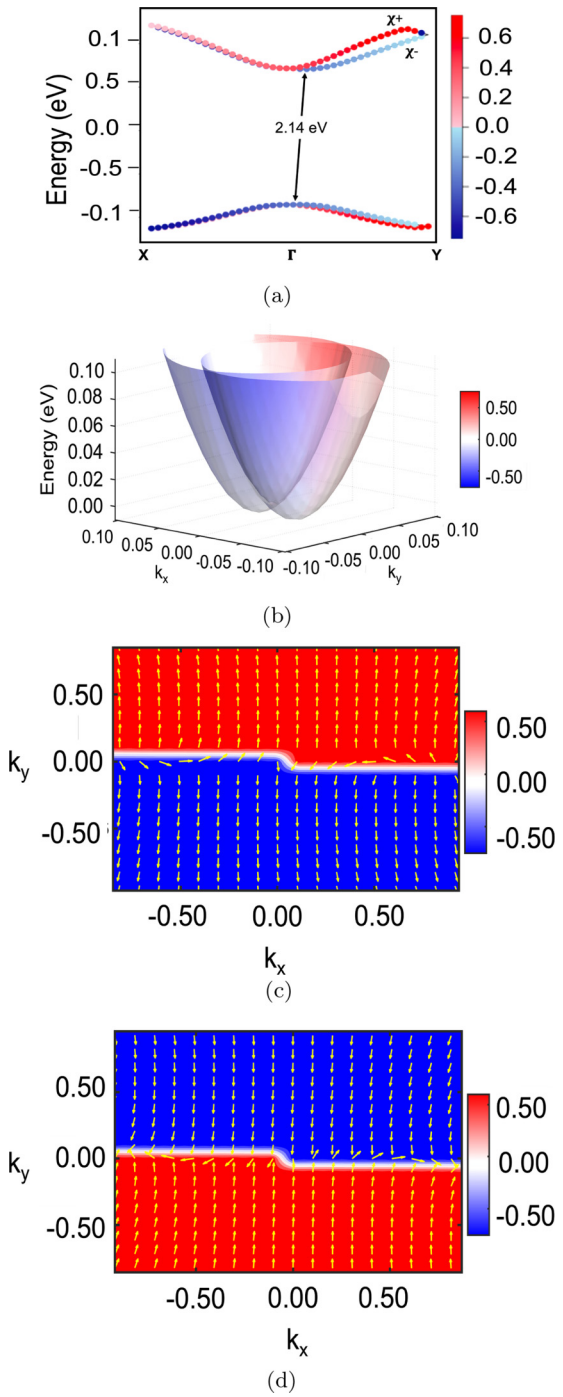

FIG. 6. Detailed views of the band splitting for $(o\text{-}F_1PEA)_2PbI_4$ structure. (a) Projected spin components χ^+ and χ^-, calculated as $\sigma_{z,n\mathbf{k}} = \langle\psi_{n\mathbf{k}}|\sigma_z|\psi_{n\mathbf{k}}\rangle$ and represented using color (red) and (blue) on bands along $X-\Gamma-Y$ symmetry path. (b) 3D plot of the energy surface for the unidirectional band splitting observed for the $\Gamma-Y$ direction. The red and blue colors on surface indicate $\sigma_{z,n\mathbf{k}}$ components shown in color bar. The energy axis is shifted so the CBM is aligned to be 0 eV for clarity. The corresponding spin textures for (c) outer and (d) inner branches of the split bands are shown. The red and blue colors indicate the $\sigma_{z,n\mathbf{k}}$ values. The yellow arrows show the resulting$\sigma_{x,n\mathbf{k}}$ and $\sigma_{y,n\mathbf{k}}$. The spin textures are calculated with a square grid of 21 points sampled along $X-\Gamma-Y$ direction using PBE+SOC level of theory.

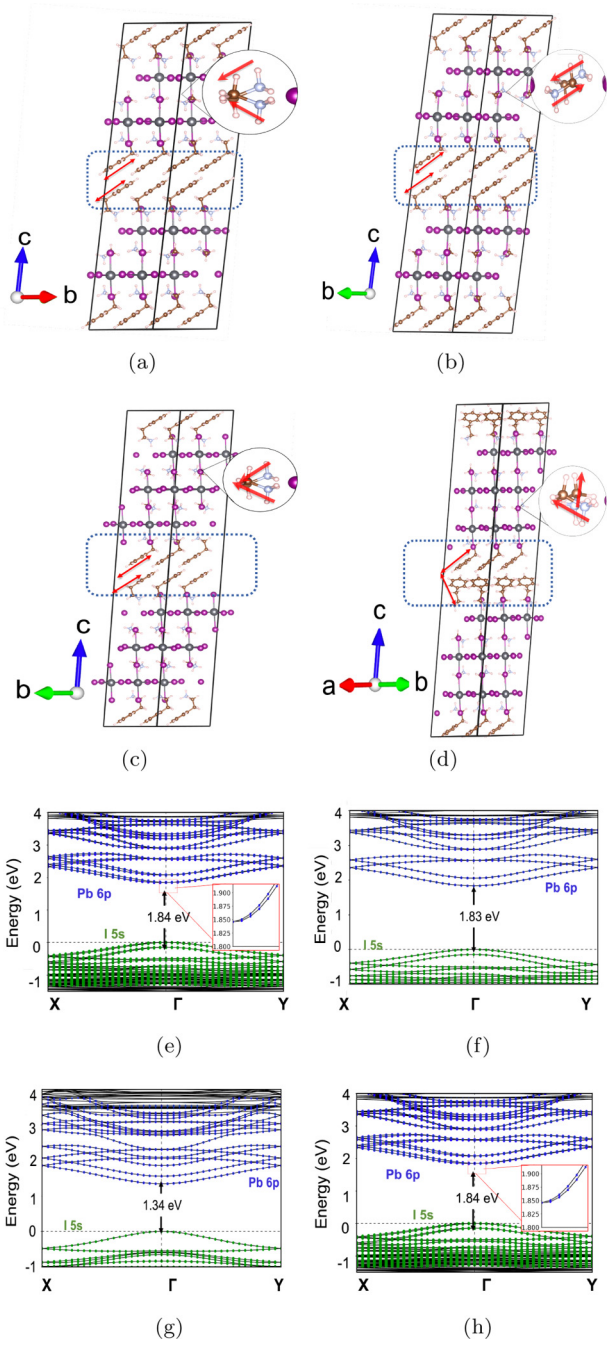

FIG. 7. Supercell structures for (a) $n=2$ $PEA_2MAPb_2I_7$:MA-A, (b) $n=2$ $PEA_2MAPb_2I_7$:MA-B, (c) $n=3$ $PEA_2MA_2Pb_3I_{10}$:MA-A, and (d) $n=3$ $PEA_2MA_2Pb_3I_{10}$:MA-C. The dotted boxes around the spacer cations highlight the mutual orientations of PEA molecules in the supercell. Corresponding band structures along $X-\Gamma-Y$ high symmetry k-path are also shown for (e) $n=2$ $PEA_2MAPb_2I_7$:MA-A, (f) $n=2$ $PEA_2MAPb_2I_7$:MA-B, (g) $n=3$ $PEA_2MA_2Pb_3I_{10}$:MA-A, and (h) $n=3$ $PEA_2MA_2Pb_3I_{10}$:MA-C.

SOC-induced band splitting [33], which is referred to as the persistent-type spin texture (PST), the corresponding spin texture shows unidirectional features as shown in Fig. 1(e). In this case, the corresponding momentum-independent (in x or y directions) spin texture can be attributed to having equal

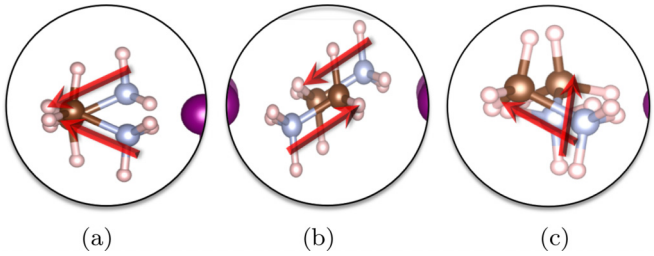

FIG. 8. Dipole orientations of two adjacent methyl ammonium (MA) cations are shown using red arrows for (a) MA-A, (b) MA-B, and (c) MA-C arrangements. In (a) and (c), the dipole moments are directing towards and away from each other, respectively, while for (b), the dipoles in MA cations are aligned in antiparallel.

magnitudes of Rashba and Dresselhaus effects, such that $\frac{\alpha_{PST}}{2} = \alpha_D = \pm\alpha_R$ [30].

III. COMPUTATIONAL DETAILS

All the 2D HOIP geometries in this paper are aligned such that c the axis corresponds to the [001] stacking axis. The inorganic layer of 2D HOIPs can be classified in terms of PbI octahedral tilts, commonly referred to as Glazer modes [22]. These modes changes the global space group, affecting SOC-induced phenomena and phase transitions [36]. As shown in Fig. 2(f), Glazer modes can be classified as rotational modes along any given lattice vectors. They are primarily of two types, categorized with respect to a major axis [001] and with respect to the adjacent octahedra. These modes make HOIPs exceedingly sensitive to the supercell in calculations. To model a 2D HOIP geometry using the periodic boundary conditions, it is imperative to choose a supercell that is large enough to include the correct Glazer mode configurations. For example, a supercell expansion with odd-size supercell expansion incorrectly shows no distortion off Wyckoff positions [37]. Following the above analysis, we use the 2×2 lateral supercell for modeling all $n = 1, 2, 3$ layered HOIPs.

All first-principles electronic structure calculations are performed using the density functional theory (DFT) implemented in the all-electron FHI-aims code [9,38]. These supercells include (a) 376 atoms and 3552 electrons for $n = 1$, 472 atoms and 5504 electrons for $n = 2$, and 568 atoms, and 7584 electrons for $n = 3$ HOIPs. Geometry optimizations are performed with the regular 4×4×2 k-point sampling of the Brillouin zone (BZ) of the supercells. We use Perdew–Burke-Ernzerhof (PBE) [39] functional together with the Tkatchenko-Scheffler (TS) pairwise dispersion correction [40] for the geometry optimization, and a residual energy tolerance of 0.005 eV. The optimized structures agree with the experimental measurements within ∼0.1% for the lattice vectors a and b and within ∼1.54% for the c lattice vector for all the geometries (as shown in Supplemental Material Table S1 in Ref. [41]).

Using the optimized geometry, we calculate the electronic structure using the Heyd Scuseria Ernzerhof (HSE06) [42] hybrid XC functional, with the default parameters $\alpha = 0.25$ and $\omega = 0.11$ bohr^{-1} [43]. We calculate the band

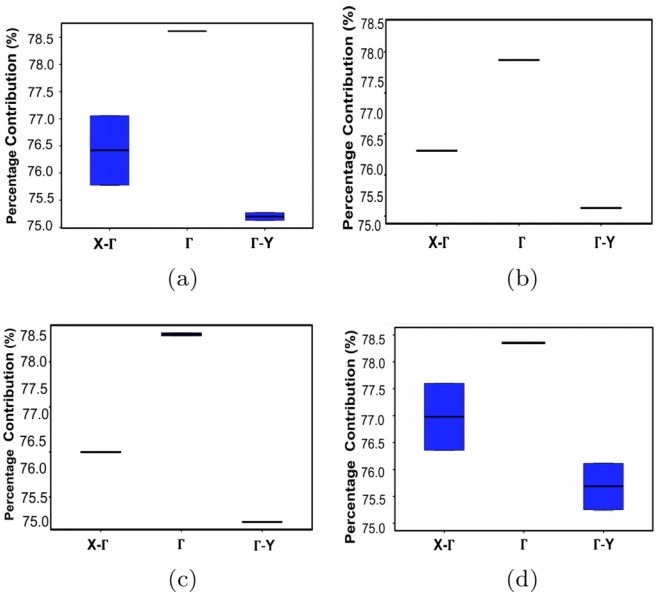

FIG. 9. Percentage contributions of Pb atomic orbitals to the conduction band minimum (CBM) states are shown for a k-point off $X - \Gamma$ direction by 0.072 Å^{-1} for (a) $n = 2$:MA-A, (b) $n = 2$:MA-B, (c) $n = 3$:MA-A, and (d) $n = 3$:MA-C. The equal magnitudes of the Pb contributions to the four CBM states are shown as black lines. The blue rectangle indicates a varying degree of contributions from different Pb atoms to the CBM states.

structures by diagonalizing the SOC operator in the basis of the scalar-relativistic Kohn-Sham eigenstates with a second-order variational approach as implemented in FHI-aims code [44]. A BZ sampling of 3×3×3 is used for all band-structure calculations. We use the ntermediate settings for the numeric atomic orbital basis set in FHI-aims code [38] to calculate the band structure and spin texture. The SOC reduces the band gap by ∼0.3 eV, mostly due to the lowering of the Pb-based conduction band minimum (CBM) state [9]. The calculation shows the energy alignment of a type-Ib quantum well (type I with the larger band gap for the organic layer); details of different quantum well structures like the energy alignment for 2D HOIPs can be found in Ref. [9].

Spin texture is defined as the expectation value of Pauli matrices σ_i [19] and calculated on a denser rectangular grid of the $\mathbf{k}$ points along the high symmetry $\mathbf{k}$-paths $X - \Gamma - Y$. This subspace in the k-points is chosen near the Γ point such the parabolic band approximation remains largely valid [24]. The spin texture, $\sigma_{i,n\mathbf{k}}$, is calculated for the outer (χ^+) and the inner (χ^-) branches as

$$\langle\hat{\sigma}_i\rangle = \langle\psi_{n\mathbf{k}}|\hat{\sigma}_i|\psi_{n\mathbf{k}}\rangle = \begin{pmatrix}\psi^{\alpha*}_{n\mathbf{k}}\\ \psi^{\beta*}_{n\mathbf{k}}\end{pmatrix}^T \hat{\sigma}_i \begin{pmatrix}\psi^{\alpha}_{n\mathbf{k}}\\ \psi^{\beta}_{n\mathbf{k}}\end{pmatrix}, \tag{5}$$

where $\hat{\sigma}_i$ is Pauli spin operator and the spinors are $\psi_{n\mathbf{k},\chi^\pm}(\mathbf{r}) = \psi^{\alpha}_{n\mathbf{k}}(\mathbf{r})|\uparrow\rangle + \psi^{\beta}_{n\mathbf{k}}(\mathbf{r})|\downarrow\rangle$. In this paper, spin textures are shown only for one of two states of the inner and outer branches because both of the two degenerate states possess the same spin textures.

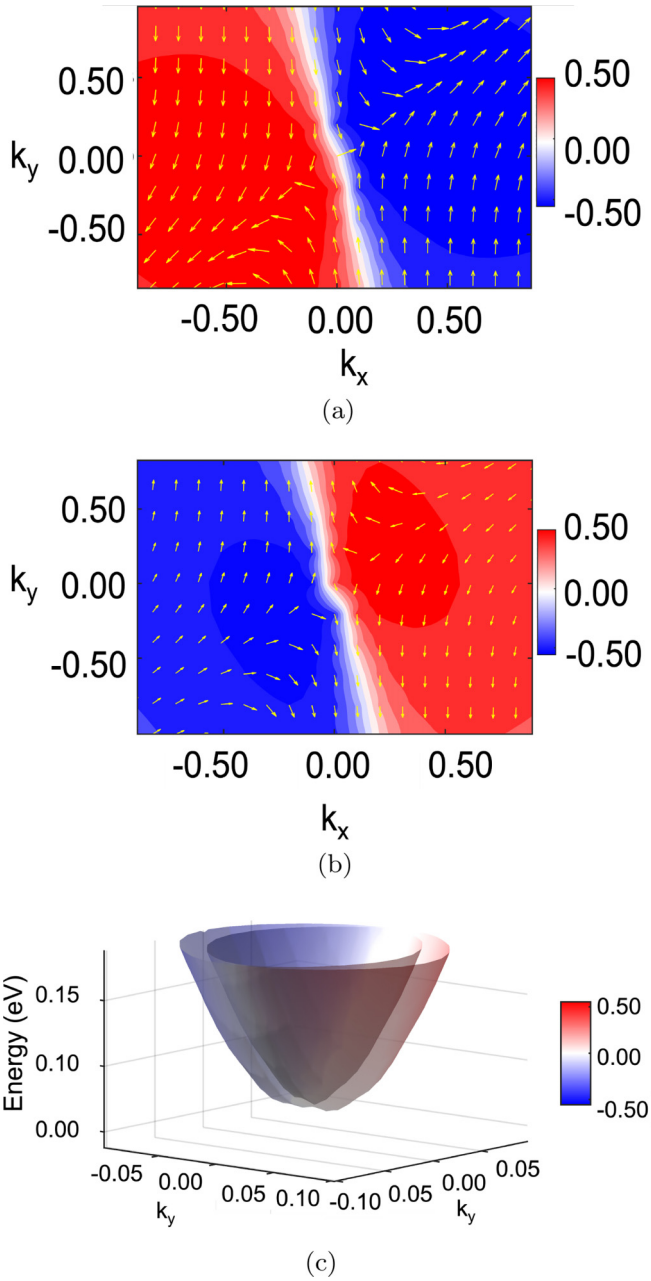

FIG. 10. Spin texture for $n = 2$:MA-A for (a) outer and (b) inner branches. Red and blue color corresponds to $\sigma_{z,n\mathbf{k}}$ component, while the yellow arrows are the result of $\sigma_{x,n\mathbf{k}}$ and $\sigma_{y,n\mathbf{k}}$ components. The spin textures are calculated with a square grid of 21 points sampled along $X - \Gamma - Y$ direction using PBE + SOC level of theory. (c) 3D plot of the energy surface for the band splitting observed. The red and blue colors on surface indicate $\sigma_{z,n\mathbf{k}}$ components shown in color bar. The energy axis is shifted so the CBM is aligned to be 0 eV for clarity.

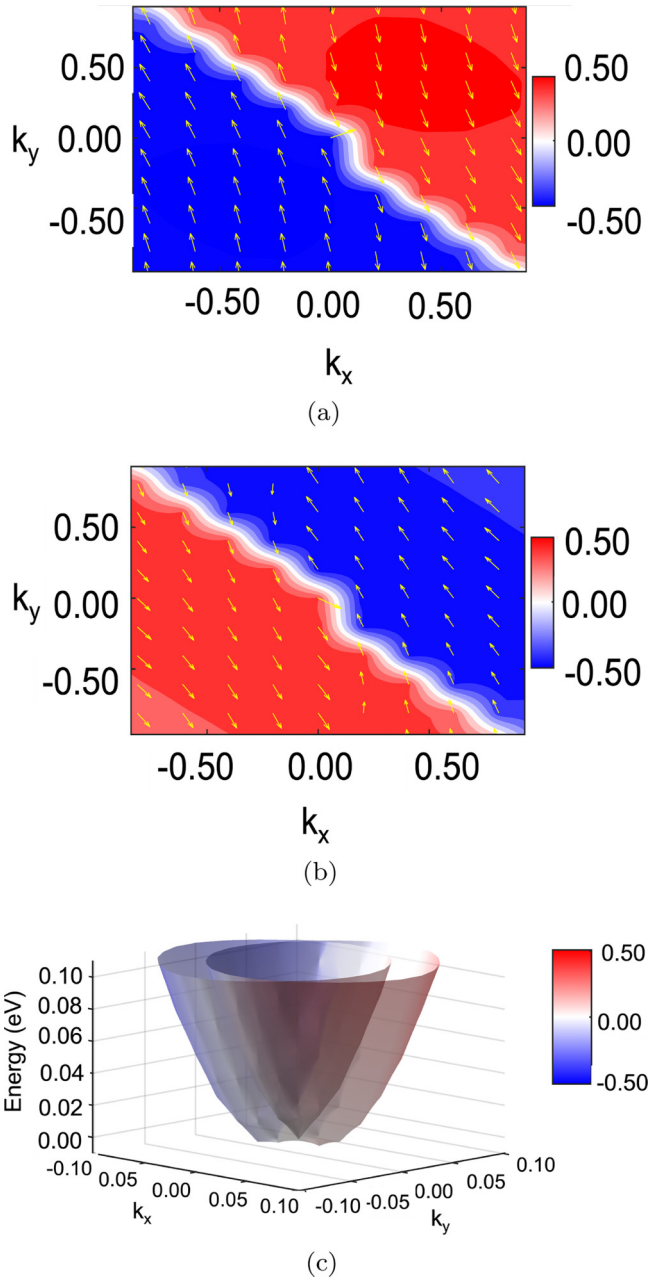

FIG. 11. Spin texture for $n = 3$:MA-C of the spins in the (a) outer and (b) inner branches. Red and blue colors correspond to $\sigma_{z,n\mathbf{k}}$ component, while the yellow arrows are the resultant of $\sigma_{x,n\mathbf{k}}$ and $\sigma_{y,n\mathbf{k}}$ components. The spin textures are calculated with a square grid of 11 points sampled along $X - \Gamma - Y$ direction using PBE + SOC level of theory, due to the large size of $n = 3$ system (7584 electrons). (c) 3D plot of the energy surface for the band splitting observed. The red and blue colors on surface indicate $\sigma_{z,n\mathbf{k}}$ components shown in color bar. The energy axis is shifted so the CBM is aligned to be 0 eV for clarity.

IV. RESULTS AND DISCUSSION

A. Fluorine substitution effect in $n = 1$ $(FPEA)_2PbI_4$

In the experimentally reported $n = 1$ phenylethylammonium lead iodide, $(PEA)_2PbI_4$, with centrosymmetric P-1 global space group, the organic PEA spacer cations are positioned at an angle of 90° with respect to each other as shown in Fig. 2(a) [46]. The lack of Rashba-/Dresselhaus-type band splittings along high-symmetry k-paths in our calculation as summarized in Table I is indeed consistent with having the centrosymmetric P-1 group [47]. While the inorganic layer in $(PEA)_2PbI_4$ governs the possibility of the splittings in a

TABLE I. Global space group reported in the literature from room-temperature experiments and determined after geometry optimization using PBE+TS level of theory. The observations of band splitting for the optimized geometries are also indicated. The space group for the optimized structures are determined using Spglib code [45].

Structures	Experimental Reference	This paper	Splitting
$(p\text{-FPEA})_2PbI_4$	$P21/c$ [16]	$P21/c$	No
$(m\text{-FPEA})_2PbI_4$	$P21/c$ [16]	$P21/c$	No
$(o\text{-FPEA})_2PbI_4$	P-1 [16]	$P1$	Yes $\Gamma - Y$ $\alpha_{\mathbf{R/D}} = 0.691\,\text{eV/Å}^{-1}$
$(PEA)_2PbI_4$	P-1 [35]	P-1	No

band structure, structural changes to the organic spacers could indirectly distort octahedral PbI cages in the inorganic layer, yielding the band splitting. In recent experimental works, Hu *et al.* [16] synthesized 2-fluorophenylethylammonium lead iodide $(x\text{-FPEA})_2PbI_4$, where a fluorine atom substitutes a hydrogen atom at x=meta (m-), ortho(o-), and para(p-) positions on the PEA ring, respectively. As shown in Fig. 2, the substitutions on the benzene ring lead to different packing motifs in the organic layer of the HOIPs [16]. We examine here how these packing motifs lead to the band splitting by inducing octahedral PbI distortion in the inorganic layer. Using the experimentally determined structures from the x-ray diffraction data [16] as the starting point, the geometry optimization is performed at the PBE + TS level of DFT calculation as discussed in the Computational Details (Sec. III). To accommodate potential occurrences of the Glazer mode distortions of octahedral PbI cages, the 2×2×2 supercell is used, as the inorganic cage is highly sensitive to the computational supercell size as discussed in Sec. III [37].

In the band structures shown in Fig. 3 for the three F-substituted systems, the blue and green colors represent the contributions of Pb 6p and I 5p states, respectively. The band gap ranges from 2.10 eV for $(m\text{-FPEA})_2PbI_4$, 2.06 eV for $(p\text{-FPEA})_2PbI_4$, to 2.14 eV for $(o\text{-FPEA})_2PbI_4$. These values do not change significantly from the band gap value of 2.06 eV for the nonsubstituted $(PEA)_2PbI_4$ case. No band splittings are observed for meta- and para-substituted FPEA as shown in Figs. 3(b) and 3(d), and this observation is consistent with these structures having a centrosymmetric $P21/c$ global space group, as reported in Table I. Band structure for $(o\text{-FPEA})_2PbI_4$, however, shows the band splitting of 0.691 eV/Å along the high-symmetry k-path $\Gamma - Y$ in the BZ [Fig. 3(c)]. The geometry-optimized structure shows a $P1$ global space group, and symmetry analysis of organic and inorganic layers further confirms a $P1$ and C_2 space group for respective sublattices. The details of relaxed parameters are included in Table S1 in the Supplemental Material [41]. The presence of a C_1 rotation as the primary symmetry operation leads to an ambiguity in identifying the source of the asymmetry and there are no specific spin textures associated like those of Rashba/Dresselhaus or PST [34]. The direction of the band splitting corresponds to the [0 1 0] direction of the structure (lattice vector b) in Fig. 2(e). And no band splitting is observed along $\Gamma - X$, which corresponds to the reciprocal lateral plane of the inorganic sublattice (i.e., lattice vector a). No band splitting is observed along $\Gamma - Z$, which corresponds to the stacking direction, given by lattice vector c (i.e., [0 0 1]).

The band splitting, which derives from the inorganic layers, can be attributed to a distorted packing of the PbI octahedral cages in this $(o\text{-FPEA})_2PbI_4$ as compared to $(PEA)_2PbI_4$, where the organic spacer cations facing each other at an angle of 90° [see Fig. 2(a)]. The preferred orientation of organic cations in $o\text{-}(FPEA)_2PbI_4$ leads to a preferential interaction between the organic and inorganic layer. The ammonium group of the spacer cation forms a hydrogen bond with only one of the bridging iodine atoms (shown in Fig. S1 in the Supplemental Material [41]. Hydrogen bonds are highlighted using dotted lines) and this causes a local asymmetry in atomic positions of the PbI inorganic sublattice. These unidirectional distortions in Pb-I-Pb cages have also been reported to manifest as a net electronic polarization in one direction [33].

The Pb-I-Pb bond angles are key structural parameters for quantifying the Glazer modes of PbI octahedral cages, which are responsible for the SOC-induced splitting [48,49]. The work by Jana *et al.* [32] has shown that the difference between the two unique sets of Pb-I-Pb angles [represented as β and β' in Fig. 2(f)] can be used to quantify in-plane and out-of-plane distortions. As shown in Fig. 4, of all cases with and without fluorine-substituted spacer cations, it is only $(o\text{-FPEA})_2PbI_4$ that has significant lateral angle differences, indicating the loss of local centrosymmetry of PbI octahedral cages. To connect this structural distortion to the band splitting observed, we utilize the Mulliken analysis [50] to identify the atomic contribution of the electronic states near the CBM, as in Refs. [51,52]. For the particular supercell used in this paper, the CBM states are quadruply degenerate without the SOC-induced splitting. Figure 5 shows variations in the percentage contribution from Pb 6p states to these CBM at and near the Γ point in the BZ. For $(o\text{-FPEA})_2PbI_4$, contributions of Pb 6p states to the CBM states are not uniform because of the structural asymmetry, lifting the degeneracy in the Γ-Y direction. At the same time, the equal contributions of Pb 6p states for $(m\text{-FPEA})_2PbI_4$ and $(p\text{-FPEA})_2PbI_4$ further highlight the local symmetric environment. The global space group alone does not give the overall picture of the SOC-induced splitting [23], and our calculations here show how the seemingly minor difference in the organic spacer molecules can lead to the band splitting indirectly via distorting PbI octahedral cages.

Having described how the SOC-induced splitting derives from the local distortion of octahedral PbI cages in $(o\text{-FPEA})_2PbI_4$, let us now discuss implications of the SOC-induced effect on the electronic spin structure. For this

TABLE II. Summary of $n = 2$, 3 layered 2D HOIPs studied. The observation of band splitting as well as their spacer cation arrangements and methyl ammonium (MA) arrangements (see Fig. 8) are indicated.

Compound	Spacer cation arrangement	MA arrangement	Splitting
$n = 2$ $PEA_2MAPb_2I_7$[26]	Parallel	MA-A	Yes $X - \Gamma(\alpha_{R/D} = 0.31\,\text{eV/Å}^{-1})$
$n = 2$ $PEA_2MAPb_2I_7$ [26]	Parallel	MA-B	No
$n = 3$ $PEA_2MA_2Pb_3I_{10}$[26]	Parallel	MA-A	No
$n = 3$ $PEA_2MA_2Pb_3I_{10}$ [61]	Perpendicular	MA-C	Yes $X - \Gamma(\alpha_{R/D} = 0.45\,\text{eV/Å}^{-1})$ $\Gamma - Y$ $(\alpha_{R/D} = 0.26\,\text{eV/Å}^{-1})$

orthosubstituted structure, Fig. 6(a) shows the expectation value of σ_z along the $X - \Gamma - Y$ k-path in the band structure. Let us focus on the inner and outer branches of the band structure formed for the CBM (which mainly derives from Pb $6p$ states), shown in red and blue circles, respectively. The band splitting is observed only for the $\Gamma - Y$ direction but not for the $X - \Gamma$ direction. Figure 6(b) shows the inner and outer branches of this energy splitting in the momentum space around the Γ point, along $-Y - \Gamma - Y$ (k_y) and $-X - \Gamma - X$ (k_x) high-symmetry k-paths. It shows double minima in the k_y axis along the $-Y - \Gamma - Y$ direction, indicating a breakdown of the Kramer's degeneracy. This band splitting is consistent with the unidirectional asymmetry of the inorganic lattice in the lateral direction [30,33], given by the nonzero difference in the opposite Pb-I-Pb angles (i.e., δ_{ac}) as shown in Fig. 4. At the same time, the largely symmetric local environment, indicated by the opposing Pb-I-Pb angle difference, δ_{bd}, yields the degeneracy along the $-X - \Gamma - X$ high symmetry k-path. To gain insights into the SOC-induced band splitting observed, the spin textures for the inner and outer branches are calculated and shown in Figs. 6(c) and 6(d). The red and blue colors in these spin texture plots are expectation values of σ_z, which correspond to the polarization in the stacking axis [001] direction. The yellow arrows in the spin texture correspond to the resulting σ_x and σ_y values. For both inner and outer branches, the yellow arrows are aligned parallel to the k_y direction, but their directions change at $k_y = 0$. Furthermore, the sign of σ_z values also change across the k_y direction, creating a polarized σ_z. These features of spin texture abide well with momentum-independent-type spin splitting, as also seen in Refs. [29,53]. Hence, the spin textures on the k_x and k_y lateral plane are parallel to only one of the k-directions, unlike those associated with Rashba/Dresselhaus splitting as shown in Figs. 1(d) and 1(c). Rather, it is best characterized as the PST, shown in Fig. 1(e). Indeed, such unidirectional band splitting has been previously observed in some 2D HOIPs like Bz_2PbCl_4 (Bz = benzylammonium) [54], GaAs/AlGaAs [55,56], and InGaAs/InAlAs [57,58]. This type of unidirectional band splittings with the corresponding spin texture that are largely k-point (i.e., momentum) independent, enables a semi-infinite spin lifetime, protecting against spin decoherence in spin field-effect transistors and spin Hall effect applications [59]. Thus, such a PST spin helix structure is highly sought after for potential applications in suppressing spin momentum scattering, further reducing Dyakonov-Perel relaxations [60].

B. Layer dependence and effect of methyl ammonium cations in $(PEA)_2(MA)_{n-1}Pb_nI_{3n+1}$

In addition to modifying the organic spacer cations as discussed in the previous section, the increasing number of layers in the inorganic sublattice changes the local symmetry of the PbI octaheral cages, especially because of MA cations within the inorganic sublattice. For 2D HOIP structures with $n = 2$ and 3, both lateral and axial Pb–I–Pb bond angles participate in distortions of PbI octahedral cages. Figure 7 and Table II summarize the experimentally reported structures we study in this paper, together with their band structures. Figure 7 shows different MA cation arrangements found in these experimentally reported structures as the insets and how they yield different electronic structures even for the same number of inorganic layers. Note also that, at room temperature, the MA cations have shown to disrupt the local centrosymmetry in 3D methyl ammonium lead iodide (MAPI), leading to the so-called dynamical Rashba splitting in perovskites [62]. As the increased number of inorganic layers accommodates, the increased degree of freedom for the MA cations becomes central to understanding PbI octahedral cage distortions. Figures 8(a)–8(c) show three different orientations for pairs of MA cations observed in the experimental structures. For convenience, the three MA cation orientations are indicated by having MA-A, MA-B, and MA-C labels so simpler notations can be sometimes used instead of the actual structural formula (e.g., n=2:MA-A instead of n=2 $PEA_2MAPb_2I_7$:MA-A). The differences in the MA cation orientation not only cause the electronic polarization to be different but also local asymmetries of PbI octahedral cages in the inorganic sublattice.

In both $n = 2$ ($PEA_2MAPb_2I_7$):MA-A ($n = 2$:MA-A), and ($PEA_2MAPb_2I_7$):MA-B ($n = 2$:MA-B) structures, the spacer cations are aligned in parallel, as highlighted using the blue box in Fig. 7. Using Spglib [45] code with a threshold of 0.1 for fractional coordinates, the overall structure is determined to possess a global P1 global for $n = 2$:MA-A and P-1 for $n = 2$:MA-B, and the inorganic sublattice is found to have a local C_{2h} symmetry group for both of the inorganic lattice. Therefore, the absence of a unique rotation direction or mirror symmetry for overall C_1 symmetry makes it not possible to conclude whether the SOC-induced splitting is expected [63] for $n = 2$:MA-A structures. Both $n = 2$:MA-A and $n = 2$:MA-B structures show the same band gap value of 1.8 eV. However, as shown in Fig. 7(e), only the $n = 2$:MA-A structure shows a band splitting of 0.2 meV with the splitting

TABLE III. Lateral angle difference for $n = 2$:MA-A and $n = 2$:MA-B characterized by $\theta_{i=\{a,b,c,d\},\text{layer}=\{1,2\}}$ (see Fig. 4). See Supplemental Material Fig. S2(a) in Ref. [41] for adetailed view of these angles for different layers. θ_i are the angular difference for each connected layer (e.g., $\theta_a = |\theta_{a,\text{layer}=2} - \theta_{a,\text{layer}=1}| = |153.79\text{-}149.93^\circ| = 3.86^\circ$). The opposite angle differences δ_{ac} and δ_{bd} are calculated as $|\theta_a - \theta_c|$ and $|\theta_b - \theta_d|$.

	$n = 2$:MA-A				$n = 2$:MA-B			
$\theta_{i,\text{layer}}(^\circ)$	a	c	b	d	a	c	b	d
layer=1	149.93	153.07	148.80	152.30	151.45	151.65	151.12	151.69
layer=2	153.79	147.42	151.06	148.97	151.45	151.64	151.12	151.69
$\theta_i(^\circ)$	3.86	5.65	2.26	3.33	0.0	0.0	0.0	0.0
	δ_{ac}		δ_{bd}		δ_{ac}		δ_{bd}	
	1.78		1.07		0.0		0.0	

parameter $\alpha_{\mathbf{R/D}}$ of $0.31\,\text{eV/Å}^{-1}$ in the $X - \Gamma$ direction. To understand the difference in local symmetries between $n = 2$:MA-A and $n = 2$:MA-B structures as far as the occurrence of the SOC-induced band splitting is concerned, we consider the structural disorder of the PbI octahedral cage structures. As discussed in the previous section, a disparity in the opposite Pb–I–Pb bond angles is an imperative marker for the existence of a local asymmetry [32]. For the 2D HOIPs with more than one inorganic layer, the disparities of the opposite angles in the PbI cages are summarized in Table III. Similarly to a work that used the distortion metric β as shown in Fig. 2(f) to identify the local symmetry [32], the Pb-I-Pb angles are measured in the 2D lateral plane. For each angle of the PbI octahedral cages (θ_a, θ_b, θ_c, and θ_d as shown in Fig. 4), we define collective angles such that $\theta_a = \theta_{a(\text{layer1})}\text{-}\theta_{a(\text{layer2})}$ for $n = 2$ structures with two inorganic layers. For $n = 2$:MA-B structures, differences of the collective angles opposing each other in PbI octahedral cages 0.0° for both $\delta_{ac} = |\theta_a - \theta_c|$ and $\delta_{bd} = |\theta_b - \theta_d|$, as shown in Table III. However, for $n = 2$:MA-A structures, the differences are $\delta_{ac} = 1.78^\circ$ and $\delta_{bd} = 1.07^\circ$, exhibiting local distortions of PbI octahedral cages, thus resulting in the small band splitting in $X - \Gamma - Y$ directions as shown in Fig. 7(e).

MA-A and MA-C structures of $n = 3$ ($PEA_2MA_2Pb_3I_{10}$) are shown in Figs. 7(c) and 7(d), respectively. These experimentally reported structures have different arrangements for the organic spacer cation in addition to MA cation arrangements. MA-A and MA-C structures show the band gaps of 1.34 eV and 1.59 eV, respectively. $n = 3$:MA-A is a three-layered extension of $n = 2$ ($PEA_2MAPb_2I_7$):MA-A structure, and it shows no band splitting. Whereas, $n = 3$:MA-C shows SOC-induced band splitting in $X - \Gamma - Y$ directions. Similarly to the $n = 2$ cases, we consider the structural disorder of the PbI octahedral cages for $n = 3$ cases. We again calculate the Pb-I-Pb angles projected onto the 2D plane, such that we define the collective angle from all inorganic layers as $\theta_a = \theta_{a(\text{layer1})} + \theta_{a(\text{layer3})} - \theta_{a(\text{layer2})}$. The signs in the linear combination are defined here by considering the relative direction of puckering in the PbI cages (see Supplemental Material [41] for [the detailed pictorial description, Fig. S2(a)]. Table IV summarizes the Pb-I-Pb angles of the octahedral cages. The differences of the opposing Pb-I-Pb angles in the octahedral cages are insignificantly small for $n = 3$:MA-A. However, for $n = 3$:MA-C, δ_{ac} of 11.05° and δ_{bd} of 6.46° are observed along lattice vectors a and b, respectively. These sizable local distortions of PbI octahedral cages yield the band splitting of 3 meV with R/D splitting parameter value of $0.45\,\text{eV/Å}^{-1}$ along $X - \Gamma$ direction as well as the band splitting along $\Gamma - Y$ direction with the splitting energy of 2 meV with R/D splitting parameter of $0.26\,\text{eV/Å}^{-1}$ as shown in Fig. 7(h).

To understand how these structural distortions of the PbI cages are directly responsible for the band splitting observed for $n = 2$ and 3, we again utilize the Mulliken analysis to identify the Pb $6p$ contributions of the otherwise degenerate electronic states at CBM, as done for $n = 1$ structures in Sec. IV A. Figure 9 shows contributions of Pb atomic orbitals to the CBM states. A highly nonuniform distribution is found in the $X - \Gamma$ direction for $n = 2$:MA-A [indicated by the blue-colored band in Fig. 9(a)], for which the band splitting is observed [Fig. 7(e)] and asymmetric Pb atoms constitute the distorted PbI cages (Table III). For the $n = 2$:MA-B [Fig. 9(b)] structure, Pb atoms contribute uniformly to the CBM states because of the highly symmetric PbI cages, and no band splitting is expected. This is also the case for $n = 3$:MA-A [Fig. 9(c)], which shows no band splitting. For $n = 3$:MA-C structures, however, Fig. 9(d) shows a nonuniform distribution in both $X - \Gamma$ and $\Gamma - Y$ directions. This analysis therefore further underscores how the octahedral PbI cage symmetry is central to understanding and how organic spacer and MA cations indirectly but significantly impact the band splitting.

While $n = 2$:MA-A and $n = 3$:MA-C structures show the band splitting, the intriguing PST is not observed for these cases. The σ_z component of spin polarization of the inner and outer branches for $n = 2$:MA-A is shown in Figs. 10(a) and 10(b), respectively. Those for the $n = 3$:MA-C structure are shown in Figs. 11(a) and 11(b) for the inner and outer branches, respectively. For both structures, σ_z shows polarization of the spin texture and the helical pattern is consistent with a mixed Rashba-/Dresselhaus-type splitting for which $\Omega(\mathbf{k})$ in Eq. (4) has dependence on both k_x and k_y [54]. Unlike for the $n = 1$ $(o\text{-}FPEA)_2PbI_4$ structure, there is no strict mirror symmetry (such as mirror planes) in the σ_z polarization, as seen for the PST case of this $n = 1$ structure (Fig. 6). Overall, these first-principles calculations on the experimentally reported structures show that the SOC effect from increasing the inorganic sublattice with $n = 1$, 2, and 3 is quite complex. Whether the band splitting is observed in the band structure depends indirectly on the particular arrangement of MA cations as well as on the organic spacer cations in these 2D HOIPs. The spin textures exhibit a more helical pattern of the Rashba-/Dresselhaus-type splitting unlike for

TABLE IV. Lateral angle difference for $n = 3$:MA-A and $n = 3$:MA-C, characterized by $\theta_{i=\{a,b,c,d\},\text{layer}=\{1,2\}}$ (see Fig. 4). See Supplemental Matrerial Fig. S2(a) in Ref. [41] for a detailed view of these angles for different layers. θ_i are the angular difference for each connected layer (e.g., $\theta_a = |\theta_{a,\text{layer}=2} - \theta_{a,\text{layer}=1}| = |166.36^\circ\text{-}155.31^\circ| = 11.05^\circ$).The opposite angle differences δ_{ac} and δ_{bd} are calculated as $|\theta_a - \theta_c|$ and $|\theta_b - \theta_d|$.

	$n = 3$:MA-A				$n = 3$:MA-C			
$\theta_{i,layer}(^\circ)$	a	c	b	d	a	c	b	d
layer=1	148.20	150.86	148.20	150.72	152.43	156.48)	155.18	154.86
layer=2	150.74	148.32	150.73	148.62	155.11	154.11	155.50	154.82
layer=3	161.54	161.54	161.54	161.54	152.23	144.23	152.62	145.16
$\theta_i(^\circ)$	137.40	−137.64	137.39	-137.80	155.31	-166.36	158.06	−164.52
	δ_{ac}		δ_{bd}		δ_{ac}		δ_{bd}	
	0.24		0.41		11.05		6.46	

the momentum-independent PST-type splitting observed for the $n = 1$ case, (o-FPEA)$_2$PbI$_4$.

C. Conclusion

In complex heterogeneous materials like 2D HOIPs, SOC-induced spin-polarization effect can arise from the point-group inversion asymmetry of atomic sites even when the global inversion symmetry is present [23]. In particular, the SOC effect in these HOIPs derives from the Pb atoms of distorted PbI octahedral cages in the inorganic sublattice. We investigated how the SOC-induced band-splitting depends indirectly on constituting organic motifs (i.e., spacer cations and MA cations) by examining experimentally synthesized HOIPs structures using first-principles electronic-structure calculations. In particular, we investigated the effect of (1) the packing of the organic spacer cations in HOIPs with one PbI octahedral inorganic layer [i.e., $n = 1$] and (2) the effect of methyl ammonium orientation associated with the increasing number of inorganic layers with more than one PbI octahedral cage layer [i.e., $n = 2$ and 3]. Building on the findings in Ref. [32] where the Pb-I-Pb angle differences are found to be the important factor governing the spin-splitting in 2D HOIPs, this metric is further examined in terms of the contributions by Pb atoms to the CBM states.

In the case of the $n = 1$ HOIPs, we observe that the packing arrangement of spacer organic cations, controlled by fluorine substitution location, is enough to induce the SOC-induced band splitting, which results from PbI octahedral cage distortions. Interestingly, the momentum-independent PST splitting rather than the conventional Rashba/Dresselhaus splitting is observed. For the $n = 2$ and 3 HOIPs, subtle changes in MA orientations are found to yield enough PbI octahedral cage distortions such that the SOC-induced band splitting is observed. Such an important role of MA orientations has been discussed in the literature for 3D perovskites under the notion of dynamical Rashba effect [62]. Our first-principles calculations of these experimentally reported structures of 2D HOIPs underscore the important role of these organic constituents for manipulating SOC-induced band splitting. The origin of dynamical spin splitting effect in $n \geqslant 1$ 2D HOIPs [4,64] will be investigated in future work.

ACKNOWLEDGMENTS

This work was financially supported by the National Science Foundation under Award No. DMR-1728921. The Research Computing at University of North Carolina at Chapel Hill is acknowledged for providing computational resources.

[1] M. Ren, S. Cao, J. Zhao, B. Zou, and R. Zeng, Advances and challenges in two-dimensional organic–inorganic hybrid perovskites toward high-performance light-emitting diodes, Nanomicro Lett. **13**, 163 (2021).

[2] F. Zhang, H. Lu, J. Tong, J. J. Berry, M. C. Beard, and K. Zhu, Advances in two-dimensional organic–inorganic hybrid perovskites, Energy Environ. Sci. **13**, 1154 (2020).

[3] C. C. Stoumpos and M. G. Kanatzidis, Halide perovskites: Poor man's high-performance semiconductors, Adv. Mater. **28**, 5778 (2016).

[4] L. Zhang, J. Jiang, C. Multunas, C. Ming, Z. Chen, Y. Hu, Z. Lu, S. Pendse, R. Jia, M. Chandra *et al.*, Room-temperature electrically switchable spin–valley coupling in a van der Waals ferroelectric halide perovskite with persistent spin helix, Nat. Photon. **16**, 529 (2022).

[5] L. Pedesseau, J.-M. Jancu, A. Rolland, E. Deleporte, C. Katan, and J. Even, Electronic properties of 2D and 3D hybrid organic/inorganic perovskites for optoelectronic and photovoltaic applications, Opt. Quantum Electron. **46**, 1225 (2014).

[6] W. S. Yang, J. H. Noh, N. J. Jeon, Y. C. Kim, S. Ryu, J. Seo, and S. I. Seok, High-performance photovoltaic perovskite layers fabricated through intramolecular exchange, Science **348**, 1234 (2015).

[7] T. M. Brenner, D. A. Egger, L. Kronik, G. Hodes, and D. Cahen, Hybrid organic—inorganic perovskites: Low-cost semiconductors with intriguing charge-transport properties, Nat. Rev. Mater. **1**, 15007 (2016).

[8] A. Kojima, K. Teshima, Y. Shirai, and T. Miyasaka, Organometal halide perovskites as visible-light sensitizers for photovoltaic cells, J. Am. Chem. Soc. **131**, 6050 (2009).

[9] C. Liu, W. Huhn, K.-Z. Du, A. Vazquez-Mayagoitia, D. Dirkes, W. You, Y. Kanai, D. B. Mitzi, and V. Blum, Tunable Semiconductors: Control Over Carrier States and Excitations in Layered Hybrid Organic-Inorganic Perovskites, Phys. Rev. Lett. **121**, 146401 (2018).

[10] F. Zheng, L. Z. Tan, S. Liu, and A. M. Rappe, Rashba spin–orbit coupling enhanced carrier lifetime in $CH_3NH_3PbI_3$, Nano Lett. **15**, 7794 (2015).

[11] N. A. Benedek, A. T. Mulder, and C. J. Fennie, Polar octahedral rotations: A path to new multifunctional materials, J. Solid State Chem. **195**, 11 (2012).

[12] C. R. Kagan, D. B. Mitzi, and C. D. Dimitrakopoulos, Organic-inorganic hybrid materials as semiconducting channels in thin-film field-effect transistors, Science **286**, 945 (1999).

[13] T. Ishihara, J. Takahashi, and T. Goto, Exciton state in two-dimensional perovskite semiconductor $(C_{10}H_{21}NH_3)_2PbI_4$, Solid State Commun. **69**, 933 (1989).

[14] Y. Shang, M. K. Hasan, G. J. Ahammed, M. Li, H. Yin, and J. Zhou, Applications of nanotechnology in plant growth and crop protection: A review, Molecules **24**, 2558 (2019).

[15] N. Wang, L. Cheng, R. Ge, S. Zhang, Y. Miao, W. Zou, C. Yi, Y. Sun, Y. Cao, R. Yang *et al.*, Perovskite light-emitting diodes based on solution-processed self-organized multiple quantum wells, Nat. Photon. **10**, 699 (2016).

[16] J. Hu, I. W. Oswald, S. J. Stuard, M. M. Nahid, N. Zhou, O. F. Williams, Z. Guo, L. Yan, H. Hu, Z. Chen, X. Xiao, Y. Lin, Z. Yang, J. Huang, A. M. Moran, H. Ade, J. R. Neilson, and W. You, Synthetic control over orientational degeneracy of spacer cations enhances solar cell efficiency in two-dimensional perovskites, Nat. Commun. **10**, 1276 (2019).

[17] T. Schmitt, S. Bourelle, N. Tye, G. Soavi, A. D. Bond, S. Feldmann, B. Traoré, C. Katan, J. Even, S. E. Dutton *et al.*, Control of crystal symmetry breaking with halogen-substituted benzylammonium in layered hybrid metal-halide perovskites, J. Am. Chem. Soc. **142**, 5060 (2020).

[18] A. Amat, E. Mosconi, E. Ronca, C. Quarti, P. Umari, M. K. Nazeeruddin, M. Gratzel, and F. De Angelis, Cation-induced band-gap tuning in organohalide perovskites: Interplay of spin–orbit coupling and octahedra tilting, Nano Lett. **14**, 3608 (2014).

[19] M. K. Jana, R. Song, H. Liu, D. R. Khanal, S. M. Janke, R. Zhao, C. Liu, Z. V. Vardeny, V. Blum, and D. B. Mitzi, Organic-to-inorganic structural chirality transfer in a 2D hybrid perovskite and impact on Rashba-Dresselhaus spin-orbit coupling, Nat. Commun. **11**, 4699 (2020).

[20] N. A. Benedek and C. J. Fennie, Hybrid Improper Ferroelectricity: A Mechanism for Controllable Polarization-Magnetization Coupling, Phys. Rev. Lett. **106**, 107204 (2011).

[21] C. J. Howard and H. T. Stokes, Group-theoretical analysis of octahedral tilting in perovskites, Acta Cryst. B **54**, 782 (1998).

[22] A. Glazer and H. D. Megaw, The structure of sodium niobate (T_2) at 600°C, and the cubic-tetragonal transition in relation to soft-phonon modes, Philos. Mag. **25**, 1119 (1972).

[23] X. Zhang, Q. Liu, J.-W. Luo, A. J. Freeman, and A. Zunger, Hidden spin polarization in inversion-symmetric bulk crystals, Nat. Phys. **10**, 387 (2014).

[24] M. S. Dresselhaus, G. Dresselhaus, and A. Jorio, *Group Theory: Application to the Physics of Condensed Matter* (Springer, Berlin, Heidelberg, 2007).

[25] L. Petersen and P. Hedegård, A simple tight-binding model of spin–orbit splitting of *sp*-derived surface states, Surf. Sci. **459**, 49 (2000).

[26] J. Yin, P. Maity, L. Xu, A. M. El-Zohry, H. Li, O. M. Bakr, J.-L. Brédas, and O. F. Mohammed, Layer-dependent Rashba band splitting in 2D hybrid perovskites, Chem. Mater. **30**, 8538 (2018).

[27] G. Dresselhaus, Spin-orbit coupling effects in zinc blende structures, Phys. Rev. **100**, 580 (1955).

[28] Y. A. Bychkov and E. I. Rashba, Oscillatory effects and the magnetic susceptibility of carriers in inversion layers, J. Phys. C **17**, 6039 (1984).

[29] S. D. Ganichev and L. E. Golub, Interplay of Rashba/Dresselhaus spin splittings probed by photogalvanic spectroscopy—a review, Phys. Status Solidi B **251**, 1801 (2014).

[30] L. Tao and E. Y. Tsymbal, Persistent spin texture enforced by symmetry, Nat. Commun. **9**, 2763 (2018).

[31] A. Manchon, H. C. Koo, J. Nitta, S. Frolov, and R. Duine, New perspectives for Rashba spin–orbit coupling, Nat. Mater. **14**, 871 (2015).

[32] M. K. Jana, R. Song, Y. Xie, R. Zhao, P. C. Sercel, V. Blum, and D. B. Mitzi, Structural descriptor for enhanced spin-splitting in 2D hybrid perovskites, Nat. Commun. **12**, 4982 (2021).

[33] F. Jia, S. Hu, S. Xu, H. Gao, G. Zhao, P. Barone, A. Stroppa, and W. Ren, Persistent spin-texture and ferroelectric polarization in 2D hybrid perovskite benzylammonium lead-halide, J. Phys. Chem. Lett. **11**, 5177 (2020).

[34] C. Mera Acosta, L. Yuan, G. M. Dalpian, and A. Zunger, Different shapes of spin textures as a journey through the Brillouin zone, Phys. Rev. B **104**, 104408 (2021).

[35] Y. Zhai, S. Baniya, C. Zhang, J. Li, P. Haney, C.-X. Sheng, E. Ehrenfreund, and Z. V. Vardeny, Giant Rashba splitting in 2D organic-inorganic halide perovskites measured by transient spectroscopies, Sci. Adv. **3**, e1700704 (2017).

[36] K. Aleksandrov, The sequences of structural phase transitions in perovskites, Ferroelectrics **14**, 801 (1976).

[37] X.-G. Zhao, Z. Wang, O. I. Malyi, and A. Zunger, Effect of static local distortions vs. dynamic motions on the stability and band gaps of cubic oxide and halide perovskites, Mater. Today **49**, 107 (2021).

[38] V. Blum, R. Gehrke, F. Hanke, P. Havu, V. Havu, X. Ren, K. Reuter, and M. Scheffler, Ab initio molecular simulations with numeric atom-centered orbitals, Comput. Phys. Commun. **180**, 2175 (2009).

[39] J. P. Perdew, K. Burke, and M. Ernzerhof, Generalized Gradient Approximation Made Simple, Phys. Rev. Lett. **77**, 3865 (1996).

[40] A. Tkatchenko and M. Scheffler, Accurate Molecular Van Der Waals Interactions from Ground-State Electron Density and Free-Atom Reference Data, Phys. Rev. Lett. **102**, 073005 (2009).

[41] See Supplemental Material at http://link.aps.org/supplemental/10.1103/PhysRevMaterials.7.055001 for further details.

[42] J. Heyd, G. E. Scuseria, and M. Ernzerhof, Hybrid functionals based on a screened Coulomb potential, J. Chem. Phys. **118**, 8207 (2003).

[43] J. P. Perdew, W. Yang, K. Burke, Z. Yang, E. K. Gross, M. Scheffler, G. E. Scuseria, T. M. Henderson, I. Y. Zhang, A. Ruzsinszky *et al.*, Understanding band gaps of solids in generalized Kohn-Sham theory, Proc. Natl. Acad. Sci. USA **114**, 2801 (2017).

[44] W. P. Huhn and V. Blum, One-hundred-three-compound band structure benchmark of post-self-consistent spin-orbit coupling treatments in density-functional theory, Phys. Rev. Mater. **1**, 033803 (2017).

[45] S. Ivantchev, E. Kroumova, G. Madariaga, J. Perez-Mato, and M. Aroyo, Subgroupgraph: A computer program for analysis of

group–subgroup relations between space groups, J. Appl. Cryst. **33**, 1190 (2000).

[46] K.-z. Du, Q. Tu, X. Zhang, Q. Han, J. Liu, S. Zauscher, and D. B. Mitzi, Two-dimensional lead (ii) halide-based hybrid perovskites templated by acene alkylamines: Crystal structures, optical properties, and piezoelectricity, Inorg. Chem. **56**, 9291 (2017).

[47] R. Winkler, *Spin-Orbit Coupling Effects in Two-Dimensional Electron and Hole Systems*, Springer Tracts in Modern Physics Vol. 191 (Springer, Berlin, Heidelberg, 2003).

[48] W. Li, J. Tang, D. Casanova, and O. V. Prezhdo, Time-domain ab initio analysis rationalizes the unusual temperature dependence of charge carrier relaxation in lead halide perovskite, ACS Energy Lett. **3**, 2713 (2018).

[49] G. Zhou, W. Chu, and O. V. Prezhdo, Structural deformation controls charge losses in $MAPbI_3$: Unsupervised machine learning of nonadiabatic molecular dynamics, ACS Energy Lett. **5**, 1930 (2020).

[50] R. S. Mulliken, Electronic population analysis on LCAO-MO molecular wave functions. I, J. Chem. Phys. **23**, 1833 (1955).

[51] P. Zhang, P. Bao, and J. Gao, Dipole preserving and polarization consistent charges, J. Comput. Chem. **32**, 2127 (2011).

[52] J. Li, T. Zhu, C. J. Cramer, and D. G. Truhlar, New class iv charge model for extracting accurate partial charges from wave functions, J. Phys. Chem. A **102**, 1820 (1998).

[53] S. Sheoran, P. Bhumla, and S. Bhattacharya, Emergence of cubic ordered full-plane persistent spin textures in lead-free materials, Phys. Rev. Mater. **6**, 094602 (2022).

[54] M. Kepenekian, R. Robles, C. Katan, D. Sapori, L. Pedesseau, and J. Even, Rashba and Dresselhaus effects in hybrid organic–inorganic perovskites: From basics to devices, ACS Nano **9**, 11557 (2015).

[55] J. D. Koralek, C. P. Weber, J. Orenstein, B. A. Bernevig, S.-C. Zhang, S. Mack, and D. Awschalom, Emergence of the persistent spin helix in semiconductor quantum wells, Nature (London) **458**, 610 (2009).

[56] M. Walser, C. Reichl, W. Wegscheider, and G. Salis, Direct mapping of the formation of a persistent spin helix, Nat. Phys. **8**, 757 (2012).

[57] M. Kohda, V. Lechner, Y. Kunihashi, T. Dollinger, P. Olbrich, C. Schönhuber, I. Caspers, V. V. Bel'kov, L. E. Golub, D. Weiss, K. Richter, J. Nitta, and S. D. Ganichev, Gate-controlled persistent spin helix state in (In,Ga)As quantum wells, Phys. Rev. B **86**, 081306(R) (2012).

[58] A. Sasaki, S. Nonaka, Y. Kunihashi, M. Kohda, T. Bauernfeind, T. Dollinger, K. Richter, and J. Nitta, Direct determination of spin–orbit interaction coefficients and realization of the persistent spin helix symmetry, Nat. Nanotechnol. **9**, 703 (2014).

[59] X.-Z. Lu and J. M. Rondinelli, Discovery principles and materials for symmetry-protected persistent spin textures with long spin lifetimes, Matter **3**, 1211 (2020).

[60] B. A. Bernevig, J. Orenstein, and S.-C. Zhang, Exact SU(2) Symmetry and Persistent Spin Helix in a Spin-Orbit Coupled System, Phys. Rev. Lett. **97**, 236601 (2006).

[61] I. C. Smith, E. T. Hoke, D. Solis-Ibarra, M. D. McGehee, and H. I. Karunadasa, A layered hybrid perovskite solar-cell absorber with enhanced moisture stability, Angew. Chem. **126**, 11414 (2014).

[62] T. Etienne, E. Mosconi, and F. De Angelis, Dynamical origin of the Rashba effect in organohalide lead perovskites: A key to suppressed carrier recombination in perovskite solar cells? J. Phys. Chem. Lett. **7**, 1638 (2016).

[63] U. Müller, *Symmetry Relationships Between Crystal Structures: Applications of Crystallographic Group Theory in Crystal Chemistry*, Vol. 18 (Oxford University Press, Oxford, 2013).

[64] M. Schlipf and F. Giustino, Dynamic Rashba-Dresselhaus Effect, Phys. Rev. Lett. **127**, 237601 (2021).